J. Fluid Mech. (2012), *vol.* 707, *pp.* 260–286.
doi:10.1017/jfm.2012.277

Interaction of a laminar vortex ring with a thin permeable screen

Christian Naaktgeboren[1], Paul S. Krueger[2]† and José L. Lage[2]

[1] Hydraulic Engineering, CFD, Andritz Hydro Ltd, Pointe-Claire, Québec, H9R 1B9, Canada

[2] Department of Mechanical Engineering, Southern Methodist University, Dallas, TX 75275, USA

(Received 15 November 2011; revised 1 May 2012; accepted 6 June 2012;
first published online 13 July 2012)

The canonical case of a vortex ring interacting with a solid surface orthogonal to its symmetry axis exhibits a variety of intricate behaviours, including stretching of the primary vortex ring and generation of secondary vorticity, which illustrate key features of vortex interactions with boundaries. Replacing the solid boundary with a permeable screen allows for new behaviour by relaxing the no-through-flow condition, and can provide a useful analogue for the interaction of large-scale vortices with permeable structures or closely spaced obstructions. The present investigation considers the interaction of experimentally generated vortex rings with a thin permeable screen. The vortex rings were generated using a piston-in-cylinder mechanism using piston stroke-to-diameter ratios (L/D) of 1.0 and 3.0 (nominal) with jet Reynolds numbers (Re_j) of 3000 and 6000 (nominal). Planar laser-induced fluorescence and digital particle image velocimetry (DPIV) were used to study the interaction with wire-mesh screens having surface open-area ratios (ϕ) in the range 0.44–0.79. Solid surfaces ($\phi = 0$) and free vortex rings ($\phi = 1$) were also included as special cases. Measurement of the vortex trajectories showed expansion of the vortex ring diameter as it approached the boundary and generation of secondary vorticity similar to the case of a solid boundary, but the primary vortex diameter then began to contract towards the symmetry axis as the flow permeated the screen and reorganized into a transmitted vortex downstream. The trajectories were highly dependent on ϕ, with little change in the incident ring trajectory for $\phi = 0.79$. Measurement of the hydrodynamic impulse and kinetic energy using DPIV showed that the change between the average upstream and downstream values of these quantities also depended primarily on ϕ, with a slight decrease in the relative change as L/D and/or Re_j were increased. The kinetic energy dissipation (ΔE) was much more sensitive to ϕ, with a strongly nonlinear dependence, while the decrease in impulse (ΔI) was nearly linear in ϕ. A simple model is proposed to relate ΔE and ΔI in terms of bulk flow parameters. The model incorporates the decrease in flow velocity during the interaction due to the drag force exerted by the screen on the flow.

Key words: porous media, vortex interactions

1. Introduction

In general terms, the interaction of a vortex ring with a permeable interface or screen may be expected to have basic features in common with the interaction of unsteady flows with complex boundaries. From this point of view, a vortex ring is

† Email address for correspondence: pkrueger@engr.smu.edu

representative of vortical flow features in unsteady flows in that it is readily generated by a variety of unsteady mechanisms (see the reviews of Shariff & Leonard 1992; Lim & Nickels 1995), the most common of which is sudden ejection of a jet from a tube or orifice. The permeable screen, by virtue of its convoluted and intertwined structure, is representative of structures ranging from filter media to trees or forested areas in that it allows permeation of the fluid together with resistance to the fluid motion, dissipation of kinetic energy and generation of additional vorticity.

More specifically, some practical applications involve flows with key features that may be expected to be similar to the special case of a vortex ring impinging on a permeable screen orthogonal to the symmetry axis of the ring. First, Staymates & Settles (2005) investigated the potential use of vortex rings to dislodge particles from a surface for application to trace explosive sampling. Staymates & Settles (2005) focused on an impermeable boundary, but in the case of trace sampling from clothing (as in modern airport security), it could be argued that a permeable boundary would be more representative of the physical conditions. Second, Krueger (2006) has proposed a method for measuring the propulsive power of self-propelled vehicles by means of a permeable matrix, which is designed to remove kinetic energy from the vehicle wake and absorb work done by fluid stresses. For investigations involving aquatic locomotion, the wake is expected to be populated with ring-like vortical structures. Understanding the interaction of unsteady vortical flows with permeable structures, particularly the force required to tow the porous medium behind the vehicle wake, is useful for the design and application of such a device. Clearly the permeable structures play an important role in the overall flow evolution, including kinematics and kinetic energy dissipation, for these and similar unsteady flows.

The interaction of a vortex ring with a permeable screen orthogonal to its axis also has fundamental relevance in that it is intermediate between the case of a free vortex and a vortex impinging on a solid surface (Naaktgeboren 2007; Adhikari & Lim 2009), where these limiting cases represent surface porosity or open-area ratio, ϕ, of 1 and 0, respectively. Both of the limiting cases have been studied extensively. For the case of a vortex ring impinging on an orthogonal solid surface, the diameter of the ring begins to expand and it slows as it approaches the wall. For sufficiently high Reynolds number (Cerra & Smith 1983), the interaction of the ring with the wall generates opposite-sign secondary vorticity at the wall. The Biot–Savart interaction of the primary and secondary vorticity leads to reversal of the axial motion of the primary vortex, commonly called ‘rebound’, and reversal of the radial motion, sometimes referred to as ‘reversal’ (Cerra & Smith 1983). For a strong enough vortex ring, tertiary vorticity is sometimes observed as well, which leads to more complex behaviour such as additional rebound and reversal events. A number of investigations have observed these basic features as well as instability in the secondary vorticity and eventual break down of the flow at later times (Magarvey & MacLatchy 1963; Boldes & Ferreri 1973; Yamada, Kohsaka & Yamabe 1982; Cerra & Smith 1983; Yamada, Mochizuki & Yamabe 1985; Walker *et al.* 1987; Orlandi & Verzicco 1993). The reader is directed to the review papers by Doligalski, Smith & Walker (1994) and by Verzicco & Orlandi (1996) for further details on vortex ring interaction with walls of normal incidence.

More limited work has been done on vortex ring interactions with permeable screens. The investigations of Naaktgeboren *et al.* (2005), Naaktgeboren, Krueger & Lage (2006), Naaktgeboren (2007) and Adhikari & Lim (2009) have observed many of the features observed in vortex ring interactions with impermeable walls (provided the Reynolds number is sufficiently high (Adhikari & Lim 2009)), including increase

in the vortex ring diameter as it approaches the boundary, generation of secondary and tertiary vorticity, and vortex ring rebound and reversal. The expansion of the ring as it approached the boundary was not as great compared to an impermeable wall, an effect that Adhikari & Lim (2009) attributed to the effect of the flow permeating through the screen, which could lead to the formation of a 'regenerated' or 'transmitted' vortex ring on the downstream side of the screen. Adhikari & Lim (2009) were primarily interested in the influence of ring Reynolds number (defined in terms of the ring circulation, i.e. Γ/ν) on the passage of the ring through the screen, and qualitatively identified four scenarios, with no passage of the ring for low Reynolds number and complete transmission of the incident ring through the screen for high Reynolds number. Hrynuk, Van Luipen & Bohl (2012) considered the effect of the screen rod diameter on the interaction of the screen for fixed ϕ, and observed that larger-diameter rods had a more disruptive effect on the ring evolution and reformation of the transmitted vortex ring, which they attributed to the localized wake formation behind larger-diameter rods.

While prior investigations (Naaktgeboren *et al.* 2005, 2006; Adhikari & Lim 2009; Hrynuk *et al.* 2012) provide important insight into the interaction of a vortex ring with a permeable screen, they consider only a few ϕ and the results are primarily qualitative. The present investigation seeks to experimentally quantify the effect of the screen on the kinematics (vortex trajectories) and dynamics (kinetic energy and hydrodynamic impulse) of the flow evolution for a broad range of ϕ.

2. Experimental set-up

The experimental apparatus used in this investigation is illustrated in figure 1. Vortex rings were produced in water by a piston–cylinder mechanism that was driven by a pressurized air/water vessel regulated at 14 psi (96.5 kPa). Closed-loop feedback control of a proportional solenoid valve (ASCO, model SD8202G57V) allowed control of the time-dependent piston velocity $U_p(t)$ according to a specified velocity programme. Measurements of the unsteady flow rate were taken with an ultrasonic inline flow sensor (Transonic Systems, Sensor Model ME 19 PX / Transit Time Tubing Flowmeter Model TS410) with an absolute accuracy of $\pm 4\,\%$. For all experiments, a trapezoidal velocity programme was used, in which the piston starting and stopping movements were characterized by accelerations of approximately $10\,\%$ of the jet duration, t_p, with a plateau at a maximum velocity of U_0 in between. The resulting velocity programme displaced the piston through a distance L. The cylindrical nozzle had an internal diameter D of 37.34 ± 0.25 mm and its edge was chamfered at an angle $\alpha = 7^\circ$ as shown on the diagram. The sharp angle at the nozzle exit plane allowed for sharp separation of the flow and clean roll-up of the resulting vortex ring. The radial distance of the nozzle centreline from the neighbouring boundaries (tank walls and fluid free surface) was greater than $7D$, preventing any significant interaction with these boundaries. The tested flow conditions were $L/D = 1.0$ and 3.0 (nominal) and jet Reynolds number, Re_j, of 3000 and 6000 (nominal), where Re_j is defined as

$$Re_j = \frac{U_0 D}{\nu}. \tag{2.1}$$

On average, the actual L/D were 0.05–0.1 less than the nominal values and the Re_j were within $2\,\%$ of the nominal values. The Reynolds numbers in terms of initial circulation (Γ/ν) for $Re_j = 3000$ were 2500 ± 210 and 4800 ± 320 at $L/D = 1$ and 3,

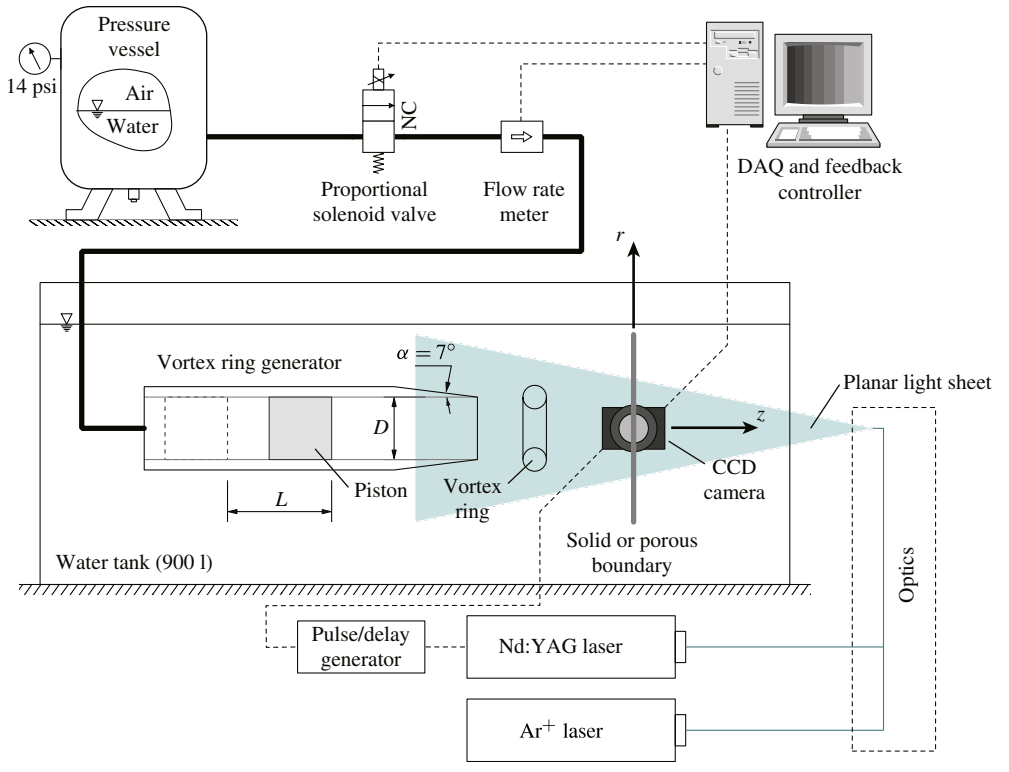

FIGURE 1. (Colour online) Schematic of the experimental set-up. NC, normally closed; DAQ, data acquisition.

respectively, and for $Re_j = 6000$ were 5700 ± 790 and $10\,000 \pm 710$ at $L/D = 1$ and 3, respectively.

2.1. *Planar laser-induced fluorescence*

To obtain qualitative information about the flow resulting from the interaction of vortex rings impinging on thin permeable screens, planar laser-induced fluorescence (PLIF) flow visualizations were used. At the nozzle exit plane, a cover with a lifting mechanism (not shown) was used for dye injection for PLIF flow visualizations. The cover was a circular disc with a central hole attached to a hose for drawing dye into the vortex ring generator tube from an elevated reservoir. The lifting mechanism used a screw actuator driven by a DC electric motor for lifting the disc at a consistent rate while minimizing the impact of the disc motion on the initial fluid motion. Covering the nozzle exit plane during dye injection ensured that only the ejected fluid was visible during the tests. Additional details about the dye injection and lifting mechanism can be found in Olcay & Krueger (2008). A coherent vertical light sheet emanating from an argon ion laser (Coherent, Model Innova 70–2) was aligned with the cylinder centreline and caused fluorescence in the disodium fluorescein dye (Walker 1987) used in the PLIF tests. The light sheet was 1.5 mm thick.

The vortex rings produced with the vortex ring generator impinged on a permeable screen (Phifer Wire, silver grey fibreglass) or an impermeable flat solid boundary oriented orthogonally to the nozzle, as shown in figure 1. The z axis of the coordinate

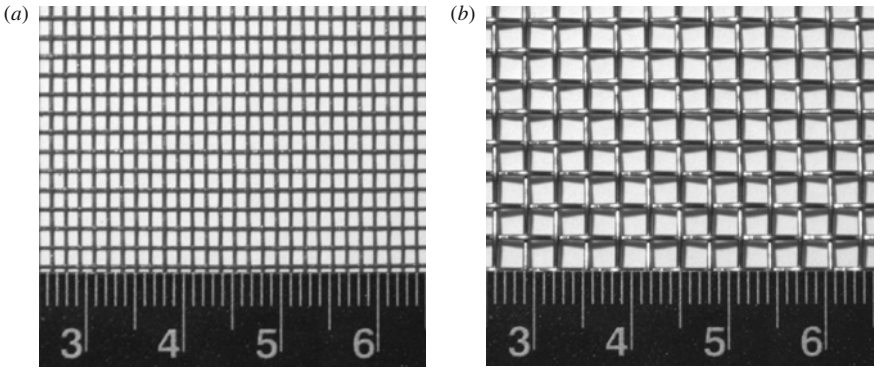

FIGURE 2. Pictures of the wire mesh permeable screens: (*a*) the fibreglass screen used in the PLIF experiments; and (*b*) one of the stainless steel screens used in the DPIV experiments (the $\phi = 60\,\%$ screen is shown). The scale at the bottom of the images is in centimetres.

system in figure 1 was aligned with the axis of the vortex ring generator and $z = 0$ was set at the mean screen/boundary location. (The mean location was used to account for irregularities in the screen/boundary location, such as small surface deformations or small inclinations in the screen/boundary angle relative to the normal.) The r axis was perpendicular to the z axis.

The boundary was approximately $3.6D$ downstream of the nozzle exit plane and greater than $15D$ upstream of the downstream tank wall. Based on visualizations of the vortex ring core diameter and trajectory, it was verified that the nozzle-to-boundary distance was sufficient to allow for vortex ring formation to be completed before interaction with the downstream boundary. Monochromatic image sequences of the flow evolution were sampled at a rate of 30 frames per second by a charge-coupled device (CCD) camera (Uniq, model UP-1830-10), with a resolution of 1024×1024 pixel^2 for all tests. To help improve the image quality near the screen, a background image with only the screen illuminated by the laser was subtracted from all flow images.

The impermeable boundary ($\phi = 0$) was standard window glass. The fibreglass permeable screen used for these qualitative results had an open-area ratio of $\phi = 58 \pm 4\,\%$. The screen had a thickness of 267 ± 13 μm and a pore aspect ratio of $1.57 \pm 3.6\,\%$, with $D/D_p = 29.4 \pm 2.6$, where D_p is the hydraulic diameter of the pore. The frontal width of the wires comprising the screen were 450 ± 50 μm. A picture of the screen is shown in figure 2(*a*). A weight attached to the bottom of the screen was used to hold the screen orthogonal to the vortex ring generator axis. The weight was large enough so that there was no observable motion of the screen during the interaction of the vortex ring with the screen. The screen was oriented so that the longer side of the rectangular pores was aligned with the vertical direction, and thus with the plane of visualization.

The fibreglass screen was only used for the PLIF results. Different permeable screens (but with a similar wire-based structure) were used for the digital particle image velocimetry (DPIV) measurements because precise control over a range of ϕ was desired for the DPIV measurements whereas the dark, opaque nature of the fibreglass screen used in PLIF results allowed for high-quality imaging of the flow near the screen while minimizing interference from laser light reflections.

2.2. *Digital particle image velocimetry*

For the DPIV tests, two Q-switched, frequency-doubled (532 nm wavelength), Nd:YAG lasers (LABest Vlite200 PIV) were used to illuminate the flow. The flow was seeded with neutrally buoyant silver-coated hollow glass particles ranging from 10 to 25 μm in diameter (Potters Industries Inc., Silvered Hollow, SH400S20). The flow was imaged at 30 Hz using the same CCD camera utilized in the PLIF experiments. Sequential image pairs were processed (giving a data rate of 15 Hz) using a 32×32 pixel^2 interrogation window at 50 % (16 pixel) overlap with a cross-correlation algorithm similar to that of Willert & Gharib (1991). The images were processed a second time with a window shifting algorithm due to Westerweel, Dabiri & Gharib (1997) for improved accuracy. The time offset between laser pulses for sequential paired images was selected to give peak pixel displacements of 8–10 pixels. The resulting flow vector fields had a spatial resolution of 1.84 mm in the axial direction and 1.88 mm in the radial direction ($0.049D \times 0.050D$) for the impermeable boundary tests, and 2.37 mm × 2.39 mm ($0.063D \times 0.064D$) in the axial and radial directions, respectively, for the permeable screen tests. The spatial resolution was worse (i.e. larger vector spacing) for the permeable screen tests because a larger field of view was used in order to image the flow downstream of the screens adequately.

The impermeable boundary used in the DPIV experiments was the same glass plate used for the PLIF experiments. To provide a range of ϕ for targets with consistent geometry, commercial 304 stainless steel woven wire meshes (McNichols Co.) were used for the permeable screens in the DPIV experiments. The wire screens were cut to a size of 12 in. × 12 in. (30.48 cm × 30.48 cm), nominal, all with the same nominal wire gauge of 0.028 in. (0.071 cm $= 0.019D$) in diameter. Four different screens were selected with twelve, eight, six and four wires per inch in both directions (i.e. nominally square pores), resulting in nominal ϕ of 44, 60, 69 and 79 %, respectively, and D/D_p of 26.6, 15.2, 10.6 and 6.62, respectively. A picture of the $\phi = 60\,\%$ screen is shown in figure 2(*b*). Although the size (see Hrynuk *et al.* 2012) and shape of the screen wires can be expected to influence the flow as well, the emphasis in this investigation is on the blockage effect provided by the screens, so the screen wire geometry is held fixed and only ϕ was allowed to vary. The nozzle-to-boundary distance was the same as for the PLIF experiments.

Although the aspect ratio of the pores in the fibreglass screen used in the PLIF experiments is different from the screens used in the DPIV experiments (1.57 versus 1.0, respectively), the pore geometry is the same (rectangular) and the wire-based screen structure is similar in both cases. As the emphasis in the PLIF experiments is on the qualitative features of the flow and visualization of how the ejected (i.e. dyed) fluid permeated the screen, rather than on quantitative one-to-one comparison with DPIV results, the difference in aspect ratio for the two cases is not considered a limiting factor in the results.

3. Flow visualization

Flow visualization of the ring interaction with an impermeable boundary was performed for comparison with the permeable screen cases using vortex rings generated from the same apparatus. From the PLIF images, spiral centres were traced on a frame-by-frame basis along the image set. A compilation of these data yields the spiral trajectories illustrated in figure 3. The location of the impermeable boundary is indicated by the white line labelled ‘solid boundary’ in the figure.

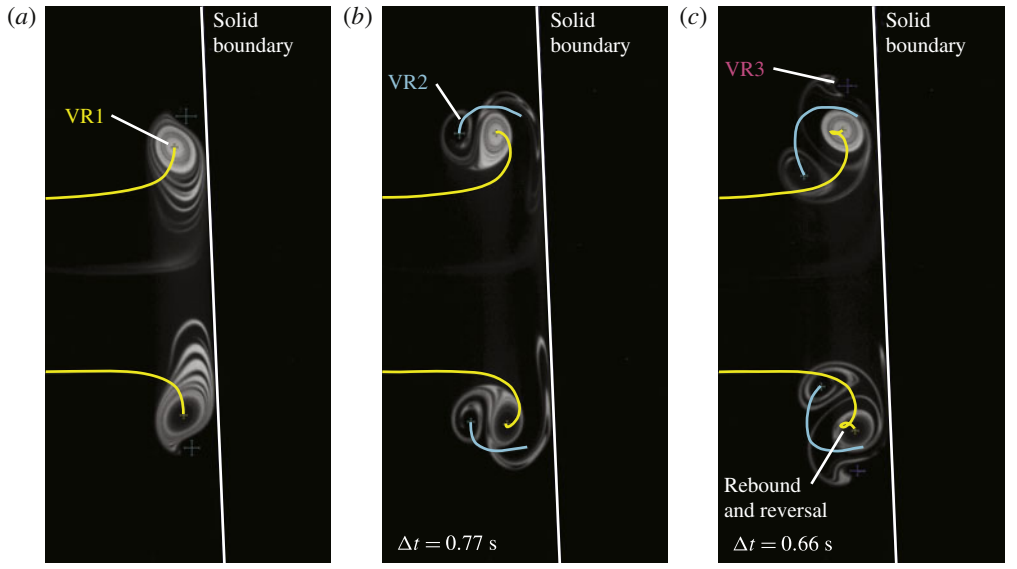

FIGURE 3. (Colour online) Vortex ring impinging on a solid boundary for $L/D = 1.0$ and $Re_j = 3000$. Light regions correspond to dyed fluid ejected from the nozzle. The indicated Δt values are the time separation from the previous panel. Lines denote the trajectories described by identifiable dyed fluid spirals.

Figure 3 illustrates many of the canonical features observed in vortex ring interactions with a solid boundary. In figure 3(*a*), the no-through-flow constraint of the solid boundary causes the primary vortex ring (VR1) to expand radially as it approaches the boundary and the vortex core to compress axially. The stretching of VR1 is evident from the radial outward motion of its spiral trajectory as the ring approaches the boundary in figure 3(*a*). At large radii, curling of the VR1 dyed fluid indicates the genesis of a secondary vortex (VR2) in figure 3(*a*), which is more apparent at later time in figure 3(*b*). The Biot–Savart interaction of VR2 with VR1 as it spirals around VR1 leads to rebound (as seen in the axial reversal of the VR1 trajectory in figure 3*b*) and reversal (i.e. change in the radial direction of motion). The combined effect of rebound and reversal produces a loop in the VR1 trajectory as seen in figure 3(*c*). The initial formation of a tertiary vortex (VR3) is also apparent in figure 3(*c*). Under ideal conditions, VR1 will continue to move in the predominantly outward radial direction (with potentially an additional rebound and reversal loop introduced by the interaction with VR3), but in the present case, the flow becomes unstable very quickly and the structures disintegrate following the sequence presented in figure 3. The high Re_j as well as the slight inclination of the solid boundary (visible in figure 3) caused by the mounting configuration used in this case led to rapid disintegration of the flow following figure 3(*c*).

Figure 4 illustrates vortex ring impingement on the permeable fibreglass screen. The regularly spaced horizontal black lines, visible only in the upstream region, are the shadows of the laser light caused by the opaque solid structures of the screen. In this sequence, many of the features observed in the interaction with the solid boundary are still present. The radial stretching of the primary vortex is observed as it approaches the screen (figure 4*a*), a secondary vortex is generated at the radially remote region of

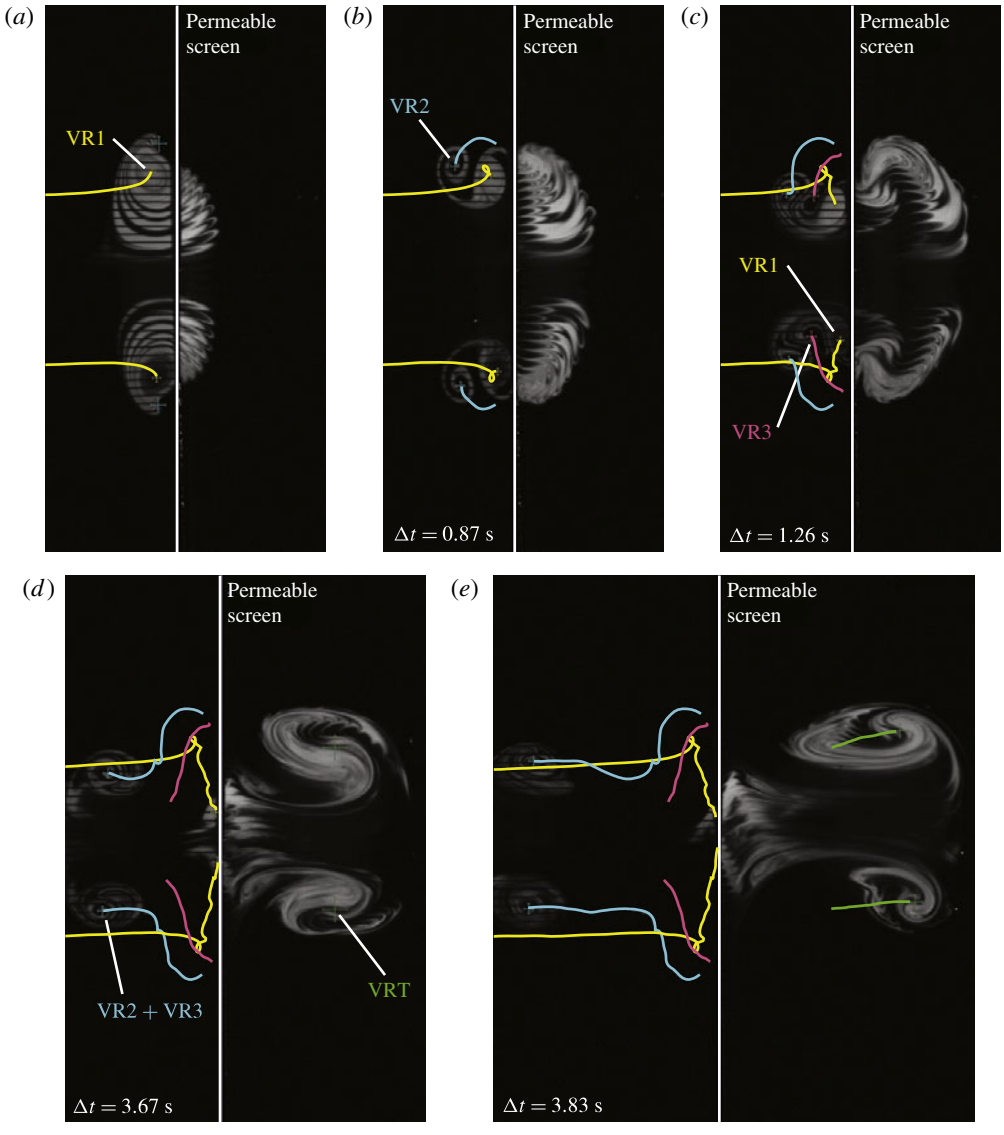

FIGURE 4. (Colour online) Vortex ring impinging on the permeable fibreglass screen for $L/D = 1.0$ and $Re_j = 3000$. The screen is located at the vertical line. The indicated Δt values are the time separation from the previous panel. Lines denote the trajectories described by identified fluid spirals.

the primary vortex interaction, the mutual interaction between VR1 and VR2 leads to classic rebound and reversal of VR1 (figure 4*b*), and at later time a tertiary vortex is formed (figure 4*c*). These features traditionally associated with vortex ring interaction with a solid boundary are present even though the boundary is highly permeable, as indicated by the early interpenetration of the ring fluid through the boundary.

A novel feature of vortex ring impingement on a permeable screen, apart from the obvious percolation of fluid downstream of the target, is the inward trajectory demonstrated by the permanent radial trajectory reversal of VR1. This is in contrast

to the generally radial outward motion of VR1 in the solid boundary case. A simple Biot–Savart analysis reveals that the induced velocity by VR2, VR3, and the forming vortical structure downstream of the target on VR1 produces an induced velocity pointing towards the original ring axis. A similar analysis for the solid boundary case reveals that VR1 reversal is due to the interaction with VR2 in this case as well. For the porous screen, however, convection of the bulk of the ring downstream of the screen pulls VR1 radially inwards. In figure 4(*d*), the VR1 spiral has shrunk to an extraordinary extent and has almost completely convected through the screen.

As a result of the inward radial trajectory of VR1, VR2 and VR3 are much closer together in the porous screen case than in the solid boundary case. Soon after formation, VR2 and VR3 have merged and are travelling upstream (figure 4*d*). While upstream motion of VR2 is possible for the solid boundary interaction, this usually occurs much later, and in figure 3 the vortices had disintegrated before significant upstream motion of VR2 was observed. The passage of fluid through the permeable screen seemed to attenuate the mechanism that makes VR2 highly unstable when a vortex ring interacts with an impermeable wall since fluid is withdrawn from the ring core, allowing it to compress radially in a more stable way. Additionally, VR2 for the permeable screen seems to be weaker and perhaps more stable (by virtue of its lower ring Reynolds number Γ/ν) than VR2 for the solid boundary. Finally, although VR2 and VR3 have the same sense of rotation, no leapfrogging was observed, as apparently viscous diffusion during merging suppressed this behaviour (Maxworthy 1972).

On the downstream side of the screen in figure 4, dyed fluid from the vortex ring is seen to penetrate the screen. The ‘sliced’ appearance of the dyed fluid downstream of the screen in figure 4(*a–c*) indicates the existence of an array of unsteady rectangular jets. Oshima & Asaka (1977) have shown that, owing to vortex merging, an array of vortex rings (from unsteady pulsed jets) recombine into a single, stable vortex ring. The close proximity between the various jets brings together regions with vorticity of opposite sign, causing strong viscous dissipation (cancellation of vorticity local peaks and valleys), while preserving the bulk axial flow near the centreline. Similar behaviour is observed downstream of the screen in the present experiments as the flow reorganizes into a new, transmitted vortex ring (VRT), as seen in figure 4(*d*,*e*).

The existence of a large-scale vortical structure downstream is not surprising given the clear penetration of the ring fluid through the screen early in the interaction. As the fluid penetrates the screen, axial fluid motion near the centreline downstream of the screen ensues, but fluid radially distant from the centreline remains stationary. Hence, the line integral of the fluid velocity around a contour containing the domain above the symmetry axis downstream of the screen will necessarily give a positive circulation, indicative of net vorticity in this domain. The transient development of the circulation in the downstream domain can be expected to lead to the roll-up of a vortical structure (transmitted vortex) instead of a continuous shear layer as might be expected for a steady jet permeating the screen. The transmitted vortex ring has a ring diameter similar to (or slightly smaller than) VR1 but a significantly slower velocity, suggesting the circulation associated with VRT is much lower than the incident ring. Nevertheless, VRT also exhibits further ambient fluid entrainment (mixing) as well as the shedding of a wake (some of the dye connected to the VRT spiral in figure 4*d* is left behind near the downstream side of the screen).

Owing to the relatively vigorous vortex rings utilized in this investigation, a VRT was observed in all cases tested and in no case did VR1 remain on the upstream side of the screen. For intermediate Reynolds number, Adhikari & Lim (2009) observed that the primary vortex core remained upstream of the screen and a vortical structure

appeared downstream, which they called a 'regenerated' vortex. For higher Reynolds number, Adhikari & Lim (2009) observed that the primary vortex penetrated the screen and merged with the downstream vortical structure, which they called a 'transmitted' vortex. In the present investigation, the VR1 core that passed through the screen clearly merged with the downstream vortical structure only for the $Re_j = 6000$ cases. (Here 'VR1 core' refers to the centre of the VR1 spiral, the location of which is represented by the VR1 trajectory in figure 4.) Nevertheless, the separation between the VR1 remnant that penetrated the screen and the newly formed downstream vortical structure decreased with increasing strength (higher L/D or Re_j) of the incident ring. Because VR1 always passed through the screen and the downstream vortical structure was clearly formed by fluid from the incident vortex (as seen by the dyed fluid it contained), the downstream vortical structure is referred to as a transmitted vortex herein, even though the incident vortex core identified by the VR1 spiral may not always have merged with the downstream vortex.

Adhikari & Lim (2009) also suggested that the induced effect of the downstream vortex on the upstream flow was a key factor in slowing the radial growth of the incident vortex, compared to the case with a solid boundary, as it approached the screen. While VRT may play some role in slowing the radial growth of VR1, the reduction in vortex stretching compared to the solid boundary case occurs well before a downstream vortex is clearly formed in the cases investigated here (compare figures 3*a* and 4*a*). A more significant factor influencing the VR1 trajectory in the present results is the through-flow allowed by the screen. In the inviscid approximation of a vortex ring approaching a solid wall, the axial slowing and radial stretching of the vortex are well described by the influence of an image vortex of equal and opposite strength on the opposite side of the boundary (Helmholtz 1867; Dyson 1893; Adhikari & Lim 2009). The image vortex enforces the no-through-flow boundary condition. For the case of a permeable screen, however, through-flow is allowed, so in the context of an inviscid model, the image vortex would have a smaller circulation than the incident vortex, and hence the radial expansion of the incident vortex would be less since the influence of the image vortex would be weaker.

The results for the remaining cases studied ($L/D = 3.0$ for $Re_j = 3000$, and $L/D = 1.0$ and 3.0 for $Re_j = 6000$) show qualitatively similar results. The main differences are that the interaction between VR1 and VR2 is much more brief and the core of VR1 has a higher tendency to merge with VRT when it emerges on the downstream side of the screen. Both effects are due to the stronger incident vortices considered in these cases. Additionally, the downstream jets that form as the flow initially penetrates the screen (see figure 4*a*) tend to be unstable or transitional, exhibiting some instability waves at the downstream edge. As a result, VRT exhibits more mixing as it forms, but the instabilities quickly die out and a smooth spiral structure emerges as VRT forms. A more detailed discussion of PLIF results for these cases is presented in Naaktgeboren (2007).

4. Quantitative measurements of flow evolution

Figures 5–7 illustrate the evolution of the azimuthal vorticity (ω_θ) obtained from DPIV for vortex rings interacting with an impermeable wall and two different permeable screens. The permeable screens were the stainless steel screens described in § 2.2. The shadows on the upstream side of the screens (similar to those in figure 4) did not significantly affect the upstream DPIV measurements because the shadow heights were only a small fraction of the interrogation window size. The upstream bulk

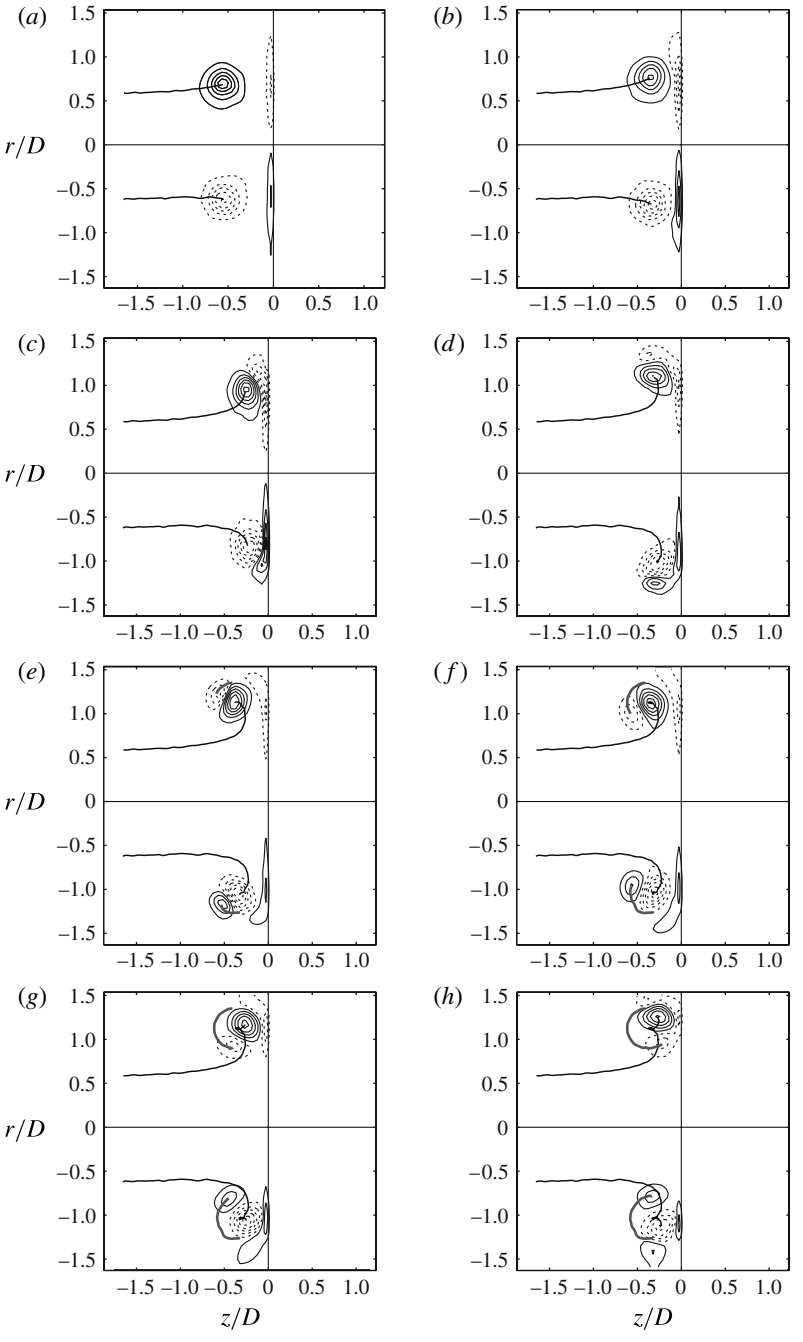

FIGURE 5. Evolution of ω_θ for $Re_j = 3000$, $L/D = 1.0$ and $\phi = 0\,\%$, with vorticity contour levels every 5.0 s^{-1} starting at ± 2.5 s^{-1}. Negative vorticity is shown as dashed contours. The time separation between panels is $\Delta t = 0.33$ s. Gaussian fitted vortex centre trajectories are shown for VR1 (black) and VR2 (dark grey).

ring properties (circulation, hydrodynamic impulse and kinetic energy) measured with and without the screens present were the same to within experimental uncertainty.

The trajectories described by the location of azimuthal vorticity peaks and valleys are shown for all cases in figures 5–7. Subgrid locations of the vorticity extrema were obtained by least-squares fitting two-dimensional Gaussian functions to the local vorticity field surrounding the peaks and valleys. For the permeable screen cases, two vertical lines bracketing the vertical axis demarcate regions in which the flow was not visually accessible. Intense laser light scattering from the screens' metallic strands, the presence of the screen, its borders and small degrees of deformation in the screen, are the causes of the lack of visual access. Correlated flow quantities in these regions were not trustworthy and have been omitted. The ring nominal parameters for figures 5–7 are $Re_j = 3000$ and $L/D = 1.0$.

Comparison of the vorticity field evolution in figures 5–7 illustrates the effect of changing the boundary porosity. Classical vortex ring rebound and reversal are evident for the solid boundary case (figure 5, $\phi = 0$). As the ring approaches the solid boundary in figure 5(*a*,*b*), the unsteady boundary layer at the wall has grown in extent and strength. This vorticity separates from the wall – panels (*c*,*d*) – and pinches off as a secondary vortex ring, as shown in panel (*e*). In figure 5(*f*–*h*) the process is repeated and VR3 pinches off. The rebound and reversal of VR1 follows directly from the mutual interaction between VR1 and VR2 in a Biot–Savart manner.

The flow evolution portrayed in figure 6 contains most of the qualitative flow features observed in the PLIF results (compare with figure 4), including radial stretching of the primary vortex ring and formation of secondary and transmitted vortices. The qualitative flow features appear relatively insensitive to the difference in pore aspect ratio for these two cases. More specifically, a small amount of radial stretching in the primary vortex ring is first observed in figure 6(*b*) as the primary vortex ring approaches the permeable screen. Figure 6(*c*) clearly shows a blob of vorticity emerging downstream of the screen – the transmitted vortex ring – as well as a VR2 that developed from the (unseen) unsteady boundary layer near the screen. The vorticity results indicate that the VRT begins forming immediately as the flow penetrates the screen and has significant strength before VR1 completely passes through the screen. This behaviour is difficult to extract from the PLIF results. Also, the VR2 developed for $\phi = 60\,\%$ is noticeably weaker than the VR2 resulting from the $\phi = 0\,\%$ interaction. This was inferred from the PLIF results, but it is quantitatively confirmed in the DPIV results. Later panels in figure 6 show VR2 wrapping around VR1 and starting to travel upstream, while the trajectory of the VRT initially contracts and then it heads downstream. VR2 decays significantly and does not go too far upstream for $\phi = 60\,\%$ before the vortex tracking algorithm loses track of it. The smaller initial radius and viscous weakening of VR2 may explain its apparently increased stability for the permeable screen results.

Radial stretching of the incident vortex ring is almost non-existent for the $\phi = 79\,\%$ sequence shown in figure 7. The same can be said with regard to secondary vortex ring formation, since VR2 was barely detected by the vortex tracking algorithm. As a result of the relatively small amount of solid surface with respect to pores for this screen, the upstream evolution of the flow is little affected by the presence of the screen. Similarly, the VRT's trajectory seems simply to be a continuation of the VR1 trajectory since the primary vortex ring has more room to pass through the screen undisturbed. Though the VRT trajectories are only slightly disturbed in these results, there is still a significant decrease in azimuthal vorticity magnitude from the primary to the transmitted vortex ring. Significantly, vortical wake structures from the screen are clearly visible in figure 7(*c*–*g*), which can be associated with the jet structures observed issuing downstream of the screen in the PLIF results. These structures were

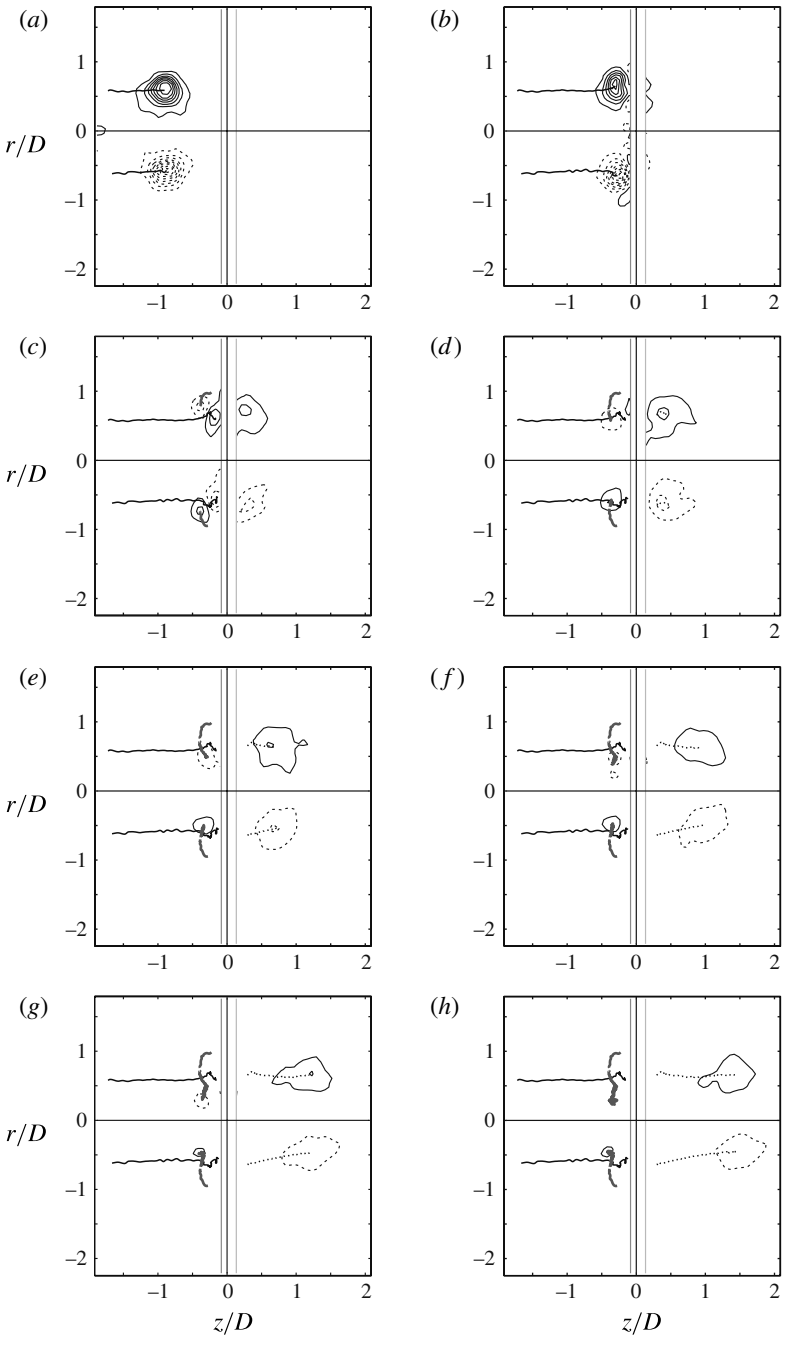

FIGURE 6. Evolution of ω_θ for $Re_j = 3000$, $L/D = 1.0$ and $\phi = 60\,\%$, with vorticity contour levels every 2.0 s^{-1} starting at ± 1.0 s^{-1}. Negative vorticity is shown as dashed contours. The time separation between panels is $\Delta t = 1.00$ s. Gaussian fitted vortex centre trajectories are shown for VR1 (black), VR2 (dark grey) and VRT (black, dotted).

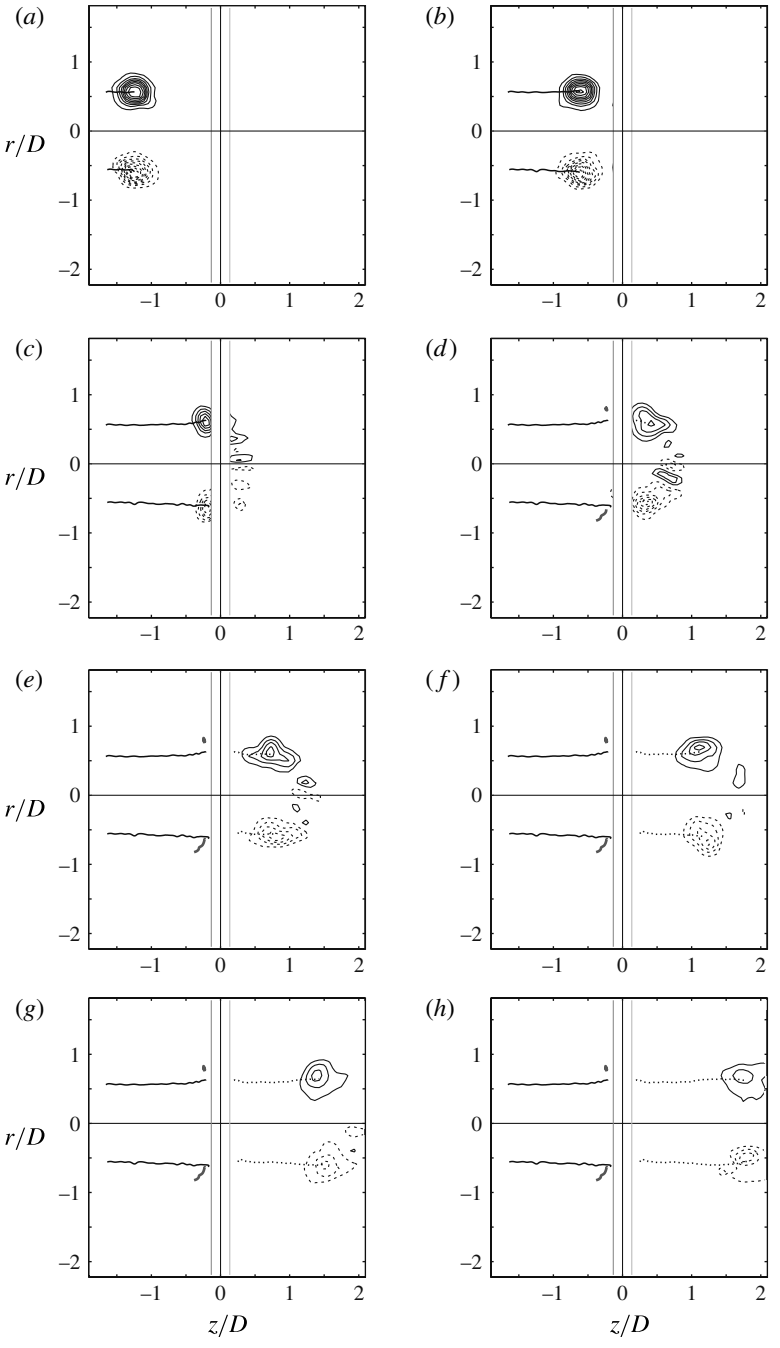

FIGURE 7. Evolution of ω_θ for $Re_j = 3000$, $L/D = 1.0$ and $\phi = 79\,\%$, with vorticity contour levels every 2.0 s^{-1} starting at ± 2.0 s^{-1}. Negative vorticity is shown as dashed contours. The time separation between panels is $\Delta t = 0.67$ s. Gaussian fitted vortex centre trajectories are shown for VR1 (black), VR2 (dark grey) and VRT (black, dotted).

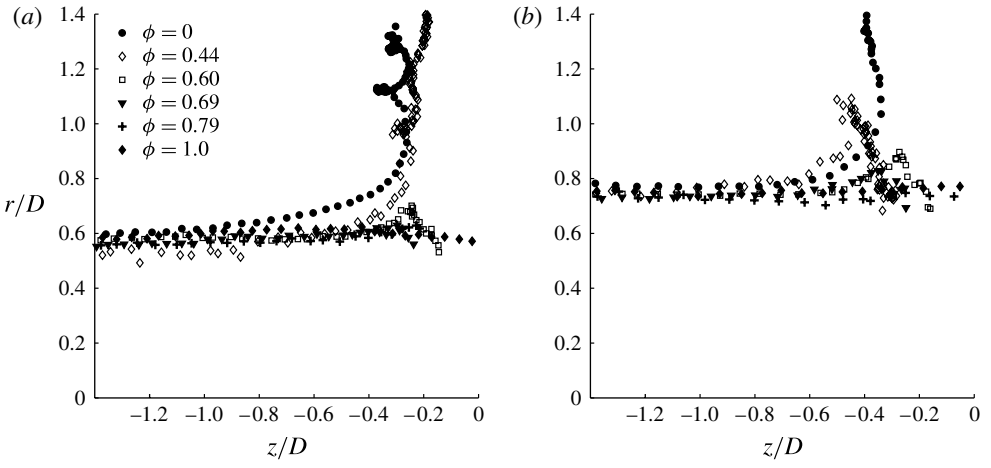

FIGURE 8. Primary vortex ring trajectories for $Re_j = 3000$: (*a*) $L/D = 1.0$ and (*b*) $L/D = 3.0$.

not observed in figure 6 for the $\phi = 60\,\%$ case because the closer spacing between the mesh strands provided increased dissipation of these structures and the DPIV resolution was comparable to the mesh spacing. For the $\phi = 79\,\%$ results, the spacing between mesh strands is 2.65 times the DPIV spatial resolution in the r direction and the structures are more readily resolved.

4.1. *Dependence of vortex trajectories on* ϕ

The vortex trajectories obtained from the DPIV vorticity results are shown in figures 8, 10 and 11 for VR1, VR2 and VRT, respectively, at $Re_j = 3000$ for $L/D = 1.0$ and 3.0. Trajectories for all ϕ where results were obtained are plotted together to allow for comparison as a function of ϕ. In particular, $\phi = 0$ (solid boundary) results are included in figures 8 and 10, and $\phi = 1$ (clear fluid) results are included in figures 8 and 11. In all cases (except $\phi = 0.44$, $L/D = 1.0$, VR1 and VR2, as discussed below), the results are for the top half of the flow domain only, with the bottom half results being similar by symmetry.

The VR1 trajectories for $L/D = 1.0$ in figure 8(*a*) show two vortex rebounds and reversals for $\phi = 0$. The first is from the interaction of VR1 with VR2 and the second is due to the influence of VR3 (see figure 5). Similarly, the lowest surface porosity case, $\phi = 0.44$, also exhibits a small rebound for $L/D = 1.0$. It should be noted, however, that the plotted trajectory for $\phi = 0.44$ is actually from the bottom vortex core because the top vortex trajectory was directed primarily towards the centreline as the vortex approached the screen, which is off the trend of the rest of the results. The bottom core, however, continues out radially much further than is expected for this ϕ (compare with figure 4). The asymmetry between the top and bottom cores in this case is associated with a slight deformation of the screen, as it was not completely flat. Slight rebound and reversal is observed for the case with $\phi = 60\,\%$ at $L/D = 1.0$. On the remaining cases in figure 8(*a*), only a small degree of radial expansion is observed, as the trajectories tend to be less disturbed by the permeable screen as ϕ is increased. The results for $L/D = 3$ in figure 8(*b*) show similar behaviour except that no rebound is observed for the $\phi = 0$ case in the field of view (which may be due to the stronger primary vortex). The rest of the cases show radial expansion tending towards rebound followed by contraction of the trajectory towards the centreline for the low ϕ

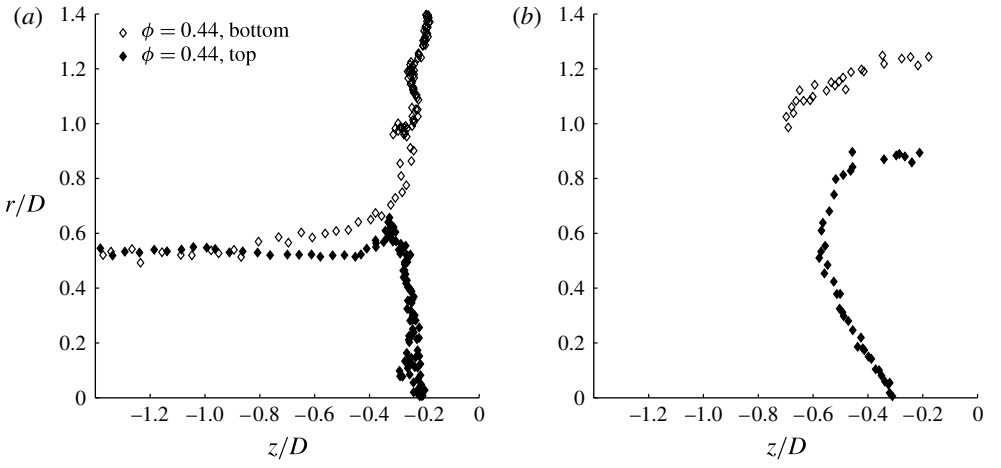

FIGURE 9. Trajectories of the top and bottom vortex ring cores for $Re_j = 3000$, $L/D = 1.0$ and $\phi = 0.44$: (*a*) VR1 and (*b*) VR2.

cases, with a clear trend towards decreased radial expansion as ϕ increases. (For $\phi = 0.44$, the top vortex core is plotted for the $L/D = 3.0$ results since the stronger vortex proved to be less sensitive to the irregularities in the $\phi = 0.44$ screen and the flow remained largely symmetric.) For $\phi = 0.79$ the primary vortex trajectory appears unaffected by the presence of the screen.

Although nearly all of the results showed good symmetry between the top and bottom vortex core trajectories (see figures 6 and 7), the $\phi = 0.44$, $L/D = 1.0$, $Re_j = 3000$ case did not. To illustrate the atypical flow evolution in this case, the trajectories of the top and bottom vortex cores for VR1 and VR2 are shown in figure 9 (VR2 trajectories will be discussed in more detail below). The VR1 trajectories (figure 9*a*) show that the bottom core shifts away from the axis rather early (around $z/D = -0.8$) and the top core shifts towards the axis slightly near the same z/D location before moving away from the axis as a result of radial stretching as the ring approaches the screen. Likewise, the top core of VR2 (figure 9*b*) forms somewhat closer to the axis than the bottom core. This behaviour indicates that the ring has tilted slightly and begun to move downwards in response to the deformation of the screen as described above. As a result, the interaction of the ring on the upstream side evolves asymmetrically, with the bottom core continuing to move away from the axis and the top core eventually moving towards the axis as the ring moves towards the screen. The transmitted vortex, however, evolved in a more symmetrical fashion.

The $\phi = 0.44$, $L/D = 1.0$, $Re_j = 3000$ case was the only one that exhibited this asymmetrical behaviour, even though some small screen deformations were present in the other cases as well. The imperfect geometry of the screen had a strong effect on this case, primarily for two reasons. First, the vortex ring for this case was the weakest, so the lower inertia of the primary ring made it more susceptible to perturbations in the screen geometry. Second, the density of solid material was highest for $\phi = 0.44$, making the influence of screen deformation more significant for this case.

The VR2 trajectory data in figure 10 show that the secondary vortex ring separates from the wall at a large radius (top portions in the figure), circumvents the primary

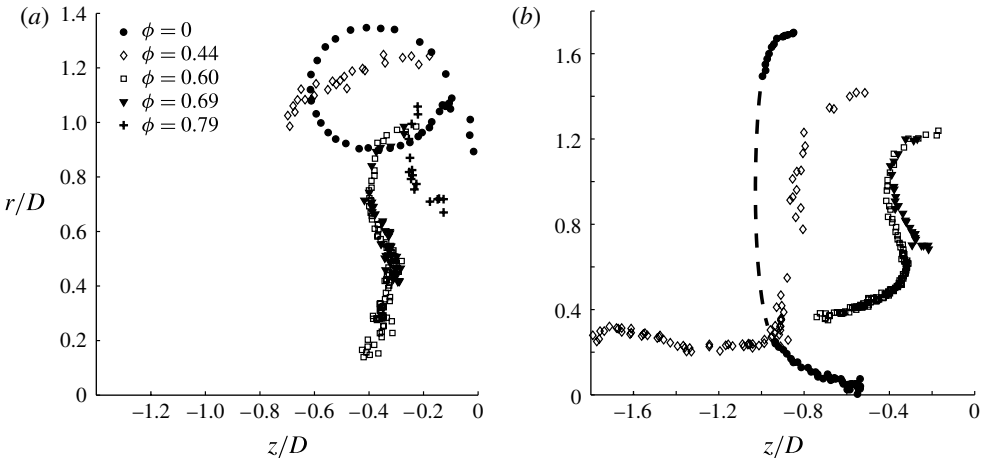

FIGURE 10. Secondary vortex ring trajectories for $Re_j = 3000$: (*a*) $L/D = 1.0$ and (*b*) $L/D = 3.0$.

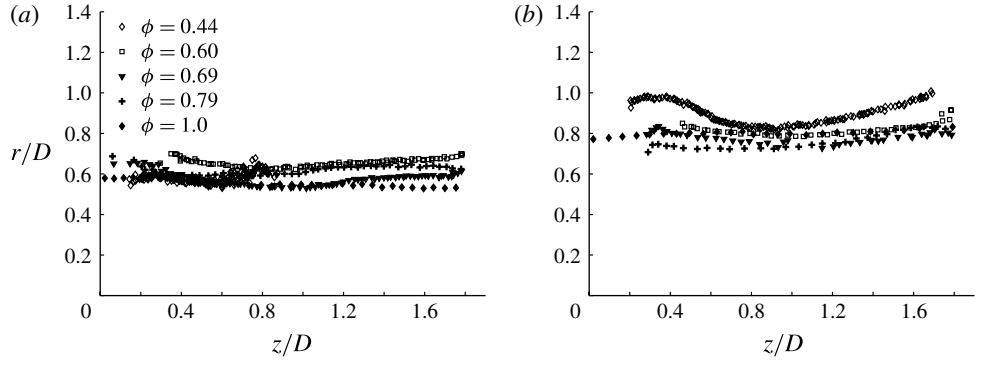

FIGURE 11. Transmitted vortex ring trajectories for $Re_j = 3000$: (*a*) $L/D = 1.0$ and (*b*) $L/D = 3.0$.

vortex ring, and goes towards the centreline, similar to the PLIF results. Note, in particular, that the trajectory for $\phi = 0$ starts out at the largest radius and, in the $L/D = 1.0$ case, loops back around to its starting point. Fewer data are available for the $L/D = 3.0$, $\phi = 0$ case because the algorithm used for finding the subgrid locations of the vorticity extrema was not able to find all of the extrema locations in this case. To help compensate, a dashed line was inserted to connect the disparate data for $\phi = 0$ in the $L/D = 3.0$ data set (see figure 10*b*), but the trajectory clearly has a larger radial extent in this case as well. As ϕ is increased, the VR2 trajectories are shifted to progressively smaller r and larger z (i.e. closer to the centre of the screen). (Note that the $\phi = 0.44$, $L/D = 1.0$ results shown are for the bottom vortex core for reasons discussed above.) This behaviour is directly tied to the VR1 motion, which is drawn down radially and forwards axially as the flow permeates the screen. No VR2 was observed for $\phi = 0.79$ in the $L/D = 3.0$ case. For the cases where data were obtained until late times, the VR2 trajectories show the secondary vortex turning upstream. The $L/D = 3.0$ results show VR2 turning upstream at larger radii and continuing upstream longer, which is associated with a stronger VR2 in these cases.

The transmitted vortex ring trajectories in figure 11 show that the transmitted vortices follow a path remarkably similar to the free vortex ($\phi = 1$) case for all ϕ. There is, nevertheless, a predominant trend of initial radial contraction, as the VRT moves away from the screen, followed by a period of expansion. The contraction and expansion seem to be largest for the $\phi = 0.44$ cases. The downstream expansion is associated with the slowing of the ring as it travels away from the screen. The initial contraction is probably related to at least two effects. First, as the VRT emerges on the downstream side of the screen, its peak vorticity is at a larger r than the upstream remnant of VR1 (see figure 6*c*), in part because VR1 is eventually drawn towards the axis as the ring passes through the screen, as discussed above. As the upstream VR1 vorticity continues to move through the screen and interacts with the VRT, the peak vorticity shifts to slightly smaller r. Second, the Biot–Savart induced velocity of the upstream VR2 on the VRT is towards the axis. Both of these effects weaken as ϕ increases and the VRT trajectories are initially more straight for large ϕ.

As the transmitted vortex travels downstream, its peak vorticity decays and its speed slows. For $\phi = 0.44$ in the $L/D = 1.0$ case, the transmitted vortex ring intensity faded away when the ring was at $z/D \approx 0.8$, after which it was no longer possible to track. The erratic path described for the ring in figure 11(*a*) for $\phi = 0.44$ is the result of uncertainties in the measurements, since the intensity of the vorticity signal approached that of the noise in the data. Therefore, the path should be understood in an average sense. Likewise, the somewhat erratic trajectory described for the highest values of z/D in figure 11 is due to slowing of the ring.

The same general incident ring trajectory trends are observed for the $Re_j = 6000$ cases, except that the trajectories are less sensitive to ϕ as Re_j increases and the trajectories are much straighter with less pronounced radial expansion. Likewise, the transmitted vortex ring trajectories follow mostly straight paths, with a certain degree of expansion as the ring moves away from the screen. The VRT for the $\phi = 0.44$ case still shows initial contraction close to the screen.

4.2. *Effect of ϕ on impulse and kinetic energy*

The influence of the permeable screen on flow dynamics is evaluated by considering the evolution of the hydrodynamic impulse, I, and fluid kinetic energy, E. For an axisymmetric flow, the hydrodynamic impulse is oriented coaxially with the axis of symmetry with magnitude

$$I/\rho = \pi \iint \omega_\theta r^2 \, \mathrm{d}r \, \mathrm{d}z, \tag{4.1}$$

where ρ is the fluid density and ω_θ is the azimuthal component of vorticity (Saffman 1992). Similarly, the kinetic energy for an axisymmetric flow is computed from

$$E/\rho = \pi \iint \boldsymbol{u} \cdot \boldsymbol{u} \, r \, \mathrm{d}r \, \mathrm{d}z. \tag{4.2}$$

As an example of the influence of the screen on the evolution of the flow dynamics, figure 12 shows the time evolution of E/ρ computed using (4.2) for the regions upstream and downstream of the screen (excluding the visually inaccessible region near the screen) for $\phi = 0.44$, $L/D = 1.0$ and $Re_j = 6000$. The E/ρ values in this figure represent the average of values computed from the data above and below the symmetry axis. The initial increase in kinetic energy in the upstream region is due to the vortex ring entering the measurement domain. When it is within the domain, the vortex ring shows an initially constant (to within experimental uncertainty) E/ρ, which

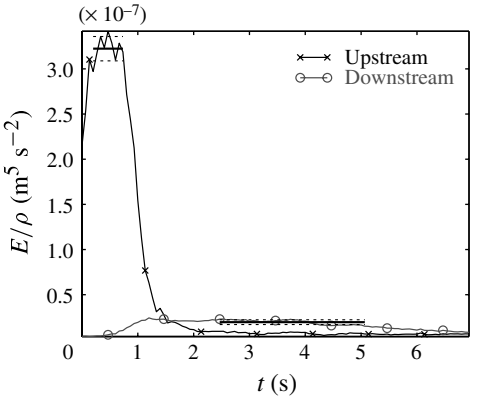

FIGURE 12. Time history of E/ρ in the upstream and downstream regions for $\phi = 0.44$, $L/D = 1.0$ and $Re_j = 6000$. Thick horizontal lines represent the time average ($\overline{E}$) and horizontal dashed lines indicate the standard deviation (σ_E) within the averaging range, which is indicated by the horizontal extent of the lines.

then decreases rapidly as it interacts with the screen for $t \approx 0.6$–1.5 s. Following this interaction, the remaining flow upstream of the screen dissipates and the kinetic energy is essentially zero beyond $t \approx 2.5$ s. In the downstream region, the kinetic energy steadily increases as the incident ring interacts with and penetrates the screen. As the transmitted ring becomes fully formed, the downstream kinetic energy stabilizes at a constant value around $t \approx 1.5$–2 s. At late time, the downstream kinetic energy begins to decay due to dissipation and/or the VRT leaving the measurement domain. Similar results are observed for the impulse.

Based on the observations from figure 12, the overall or net effect of the screen on the flow dynamics can be characterized by the difference between the average upstream, $(\cdot)_u$, and downstream, $(\cdot)_d$, values, denoted ΔI and ΔE for impulse and kinetic energy, respectively. The changes in impulse and kinetic energy were computed from the upstream and downstream values averaged over the time period when the vortex rings were in the middle 60 % of the measurement domains upstream and downstream of the screen, respectively. As with the results in figure 12, the average of values computed above and below the axis of symmetry was used to help account for any lack of axisymmetry in the flow. Additionally, any slight asymmetry in the trajectory of the vortices during the flow evolution was accounted for by locating the $r = 0$ axis midway between the positive and negative vorticity centroids when using (4.1) and (4.2) to compute $(\cdot)_u$ and $(\cdot)_d$ values. The results, normalized by the upstream values, are presented in figures 13 and 14 for impulse and kinetic energy, respectively, as a function of ϕ for all L/D and Re_j considered. The clear fluid results ($\phi = 1$) are also plotted for comparison. There are no $\phi = 1$ data shown in figure 13(b) because, owing to experimental error, ΔI is slightly negative for this case, so it is not plotted. Also, a slight irregularity in the jet velocity programme for the $\phi = 1$ case in figure 13(c) led to the formation of a small secondary vortex during jet ejection, which promoted vortex shedding and more rapid energy dissipation for this case. Because of this atypical behaviour, the $\phi = 1$ case for $L/D = 1$, $Re_j = 6000$ is not plotted in figures 13(c) and 14(c). The error bars in figures 13 and 14 represent the uncertainty in the results as determined by the standard deviation (σ) of the upstream

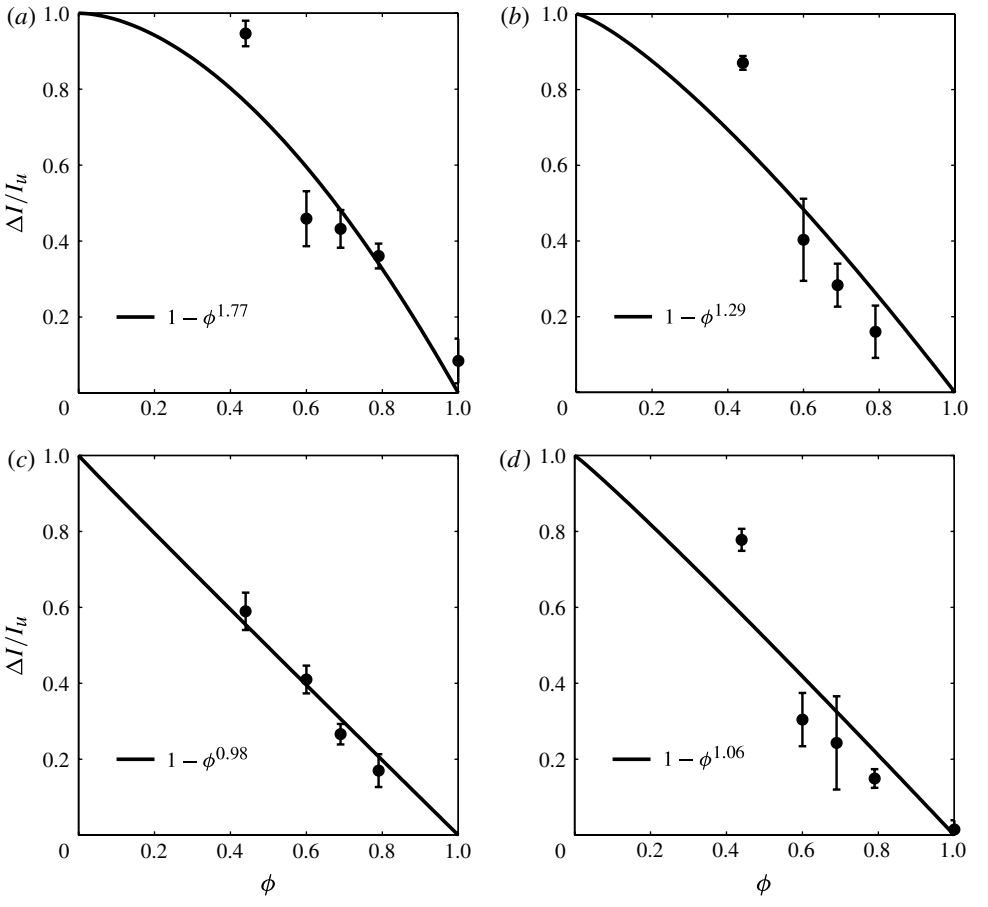

FIGURE 13. Normalized change in fluid impulse for constant nominal ring parameters as a function of screen surface porosity ϕ: (*a*) $L/D = 1.0$, $Re_j = 3000$; (*b*) $L/D = 3.0$, $Re_j = 3000$; (*c*) $L/D = 1.0$, $Re_j = 6000$; and (*d*) $L/D = 3.0$, $Re_j = 6000$. The solid line is the best-fit curve, with the equation given in each panel.

and downstream quantities. Any values deviating by more than 2σ from the mean were removed from the data set and the statistics recomputed. A least-squares best-fit curve with the functional form $1 - \phi^{\beta}$ is plotted as a solid line in the figures. The exponent β is indicated on the equation in the inset for each panel of the figures. This functional form is selected for the best-fit curve since it is the simplest form that has the proper values at $\phi = 0$ and 1.

Figures 13 and 14 show a decrease in both $\Delta E/E_u$ and $\Delta I/I_u$ as ϕ increases. The change in impulse reflects the drag force exerted on the flow by the screen, while ΔE indicates the dissipation in kinetic energy during the interaction of the vortex ring with the screen. A smaller ϕ screen is expected to have a stronger effect in both cases, as is indicated by the measurements. Nevertheless, even very open screens with $\phi = 0.79$ remove ~20–40 % of the impulse and ~40–60 % of the kinetic energy from the flow. For $\phi = 1$, ΔI should be zero (if all the vorticity is accounted for in the $(\cdot)_u$ and $(\cdot)_d$ calculations) and, for the Reynolds numbers considered, ΔE should be small. This is generally observed, except that $\Delta I/I_u$ is larger than expected for $L/D = 1$

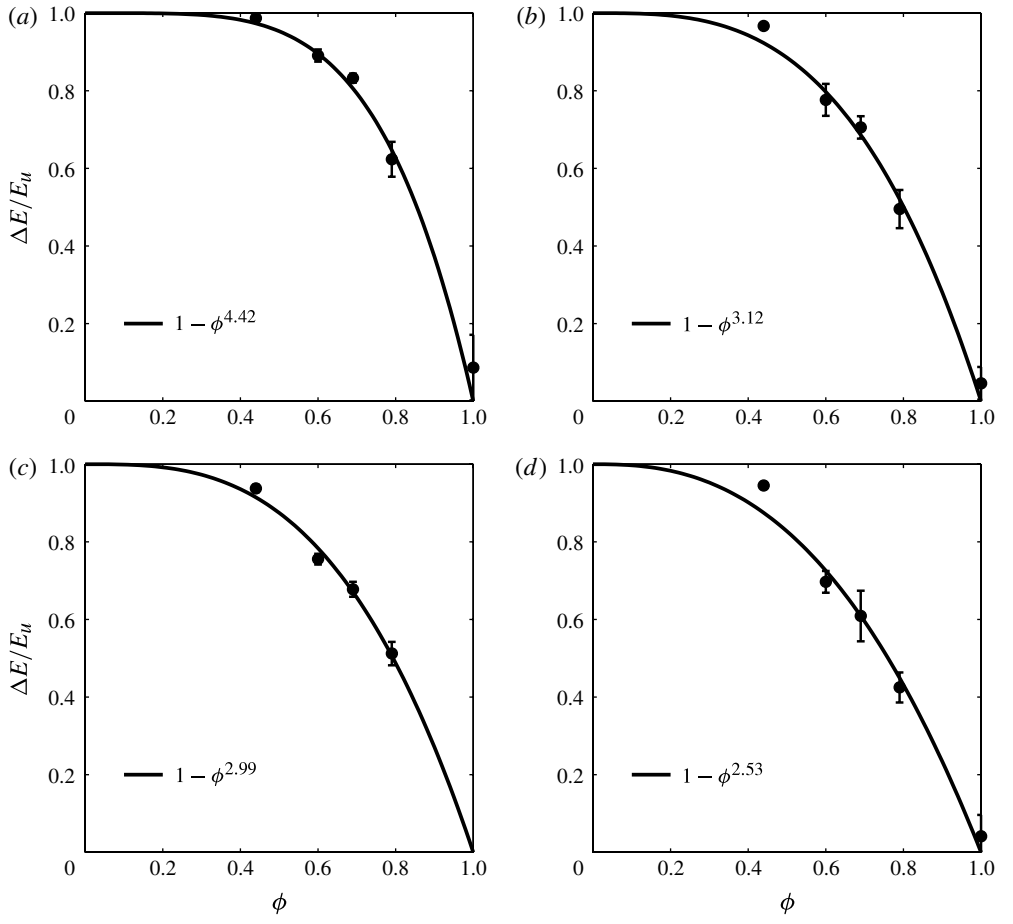

FIGURE 14. Normalized total kinetic energy dissipation for constant nominal ring parameters as a function of screen surface porosity ϕ: (*a*) $L/D = 1.0$, $Re_j = 3000$; (*b*) $L/D = 3.0$, $Re_j = 3000$; (*c*) $L/D = 1.0$, $Re_j = 6000$; and (*d*) $L/D = 3.0$, $Re_j = 6000$. The solid line is the best-fit curve with the equation given in each panel.

and $Re_j = 3000$ at $\phi = 1$ (see figure 13*a*). Nevertheless, the impulse loss at $\phi = 1$ in figure 13(*a*) is not large when the uncertainty is accounted for. Also, if any vorticity is shed from the ring during its evolution, this may not be captured in the downstream measurement, giving a non-zero ΔI.

The sensitivity of $\Delta E/E_u$ to ϕ appears to be much stronger than $\Delta I/I_u$, at least for $\phi > 0.5$. This is reflected in the highly nonlinear character of the best-fit curves for $\Delta E/E_u$, showing almost complete kinetic energy dissipation for $\phi < 0.5$, whereas the $\Delta I/I_u$ results show a nearly linear dependence on ϕ. Significantly, the best-fit curve exponent β tends to decrease as both Re_j and L/D increase. This is true for both the energy and impulse results (with the exception of $Re_j = 6000$ for $\Delta I/I_u$, which does not show a significant change in β as L/D increases from 1.0 to 3.0). This suggests that more vigorous vortex rings generated by increasing L/D and/or Re_j have a weaker *relative* interaction with the screen. This is certainly possible, since the total duration of the interaction between the screen and the vortex ring is shorter for stronger vortex rings (note the Δt dependence in (4.5)).

Figures 13 and 14 suggest that the dominant factor affecting the interaction of the vortex ring with the permeable screen is ϕ, at least for the conditions tested here. This is illustrated in figure 15, which shows $\Delta I/I_u$ and $\Delta E/E_u$ as functions of the normalized upstream values, I_u^* and E_u^*, where

$$I_u^* \equiv \frac{I_u}{\rho U_0 D^3} \tag{4.3}$$

and

$$E_u^* \equiv \frac{E_u}{\frac{1}{2}\rho U_0^2 D^3}. \tag{4.4}$$

The $Re_j = 3000$ results are plotted with filled symbols and the $Re_j = 6000$ results are shown as open symbols. With I_u and E_u normalized in this way, the effect of Re_j (adjusted by changing U_0) is effectively scaled out, with I_u^* and E_u^* depending primarily on L/D. In figure 15, the group of points clustered at lower I_u^* and E_u^* correspond to $L/D = 1.0$ and the points at higher values correspond to $L/D = 3.0$.

Overall, the results for a given ϕ (given symbol shape) in figure 15 are very similar. In most cases there is only a slight difference between $\Delta I/I_u$ for a given ϕ (figure 15*a*), and frequently any difference is smaller than the experimental uncertainty, especially for the $L/D = 3$ results (larger I_u^* values). Similar statements can be made for $\Delta E/E_u$ (figure 15*b*). Nevertheless, there is a clear separation between cases as ϕ increases from 0.44 to 1.0, indicating the predominance of this variable in determining the overall flow evolution.

4.3. *A model relating ΔE and ΔI*

To elucidate the difference in the dependence in ΔE and ΔI on ϕ and to clarify the key effects of ϕ on the flow dynamics, it is helpful to consider a simple model of the effect of the screen on E and I. To this end, observe that

$$\Delta I \equiv I_u - I_d = \int_0^{\Delta t} F_D \,\mathrm{d}\tau \equiv \overline{F}_D \Delta t, \tag{4.5}$$

where F_D is the total drag force exerted by the screen on the flow during the interaction, Δt is the duration of the interaction and the overbar denotes the time average. Then,

$$\Delta E \equiv E_u - E_d = \int_{screen} \int_0^{L_i} f_D \,\mathrm{d}l \,\mathrm{d}A \approx \int_0^{L_i} \overline{F}_D \,\mathrm{d}l, \tag{4.6}$$

where f_D is the local drag force exerted by the screen on the flow (per unit area) and L_i is the total displacement of the fluid during the interaction with the screen. Specifically,

$$\mathrm{d}l = u' \,\mathrm{d}t = \frac{u}{\phi} \,\mathrm{d}t, \tag{4.7}$$

where u' is axial component of the local pore velocity at the screen and u is the upstream axial velocity component (only the axial component is considered for simplicity, as this is the dominant flow direction). Then, assuming constant acceleration, a, to give a leading-order approximation,

$$u = \int_0^t a \,\mathrm{d}\tau \approx W_r + at, \tag{4.8}$$

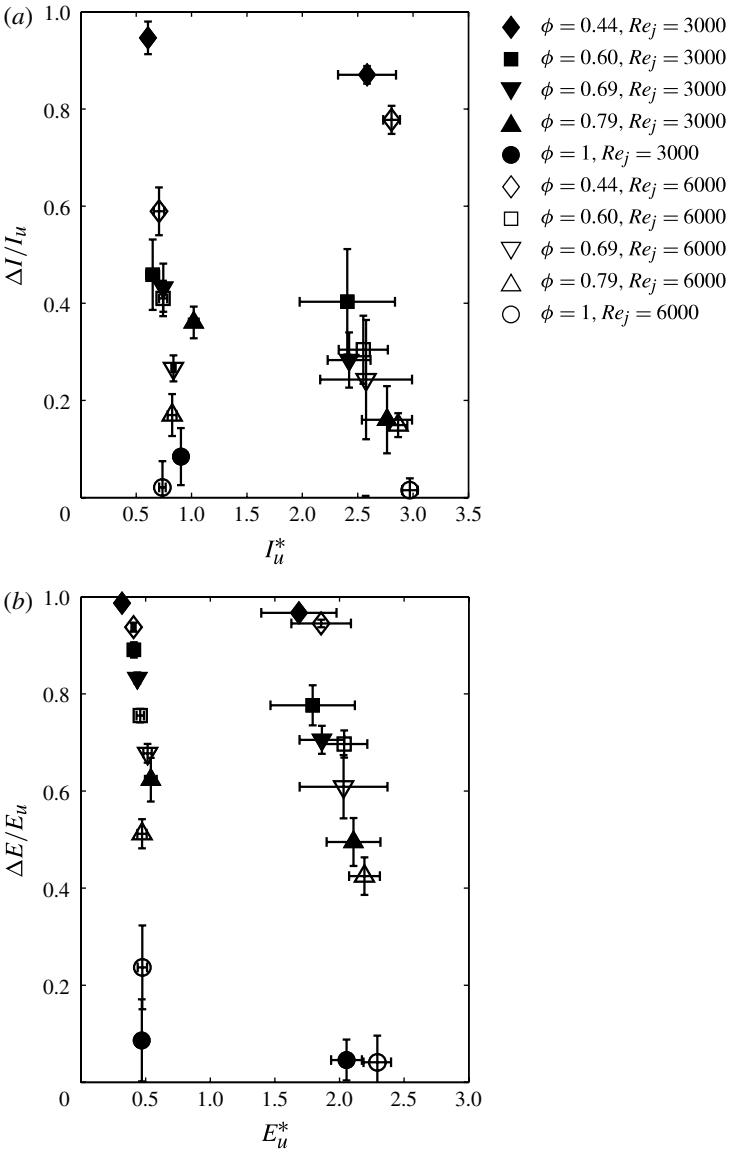

FIGURE 15. Normalized change in impulse and kinetic energy as a function of normalized initial values: (*a*) impulse and (*b*) kinetic energy.

where W_r is the initial upstream velocity of the vortex ring. Combining (4.6)–(4.8) gives

$$\Delta E \approx \frac{\overline{F}_D}{\phi} \int_0^{\Delta t} (W_r + a\tau)\, \mathrm{d}\tau = \frac{\overline{F}_D}{\phi} \left(W_r \Delta t + \frac{1}{2} a\, (\Delta t)^2 \right). \tag{4.9}$$

The acceleration a is negative, given that the vortex ring slows as it approaches the screen and its final downstream velocity is reduced compared to the initial velocity. As this deceleration is associated with the force applied to the flow by the screen, a reasonable approximation is $a \approx -\overline{F}_D/m$, where m is the total mass of fluid associated

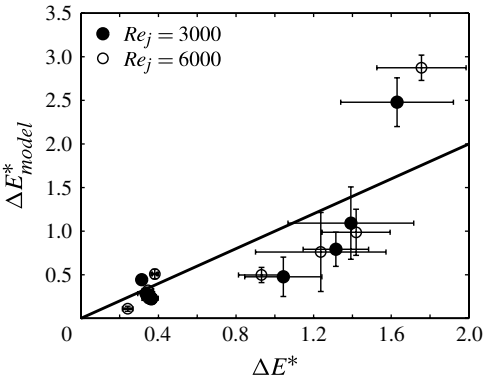

FIGURE 16. Predicted kinetic energy dissipation versus measured kinetic energy dissipation. The solid line is the best-fit line.

with the motion of the vortex ring. For the incident ring, the initial mass m_0 would include the fluid mass convected with the ring in the vortex bubble and the added mass surrounding the ring and set into motion by the convection of the ring through the fluid. In general, m will be a function of time, but since the majority of the fluid initially in the ring convects through the screen (see figure 4) and the diameter of the transmitted ring is largely unchanged (see figure 11), a reasonable leading-order approximation is $m \approx m_0$. Using this result in (4.9) gives

$$\Delta E \approx \overline{F}_D \Delta t \frac{W_r}{\phi}\left(1 - \frac{1}{2}\frac{\overline{F}_D \Delta t}{m_0 W_r}\right). \tag{4.10}$$

Then substituting (4.5) and using the fact that $m_0 W_r = I_u$ (Krueger & Gharib 2003) gives

$$\Delta E \approx \Delta I \frac{W_r}{\phi}\left(1 - \frac{1}{2}\frac{\Delta I}{I_u}\right) \equiv \Delta E_{model}. \tag{4.11}$$

Using the measured values for ΔI and I_u together with W_r determined from the measured trajectories of the incident vortex rings, ΔE_{model} is plotted versus the measured ΔE in figure 16. The values have been normalized by $(\rho U_0^2 D^3)/2$ as in (4.4). The least-squares best-fit linear curve is also shown in figure 16 as the solid line. The best-fit line happens to have a slope of 1.00, indicating that – on average – the model provides a reasonable prediction of ΔE. The $\phi = 1.0$ results are not included in figure 16 because the basis of the model (i.e. interaction of the flow with a thin screen) is not representative of this case and other effects dominate the flow.

Comparison of the predicted and measured ΔE in figure 16 shows that the model is reasonably accurate, even though it utilizes rather crude approximations. The model emphasizes the effect of the drag force from the screen and the flow deceleration on the energy dissipation process. The rough agreement between the model and measurements suggests that the model captures the dominant influence of these effects on the overall physics of the interaction. Notably, the model predicts a nonlinear dependence on ΔI and ϕ, giving an indication why a highly nonlinear dependence of $\Delta E/E_u$ is observed when $\Delta I/I_u$ has a nearly linear dependence on ϕ. Additionally, the model explicitly incorporates the slowing of the flow during the interaction with the screen. This appears as the $-\Delta I/(2I_u)$ term in the model. If this term is not present,

the model tends to overpredict ΔE significantly (except for the $\phi = 0.44$ results), suggesting that retardation of the flow is an important component of the overall interaction dynamics. However, this effect is also present in the ΔIW_r contribution to (4.11), so it is difficult to decipher the precise effect of flow retardation on the overall dynamics from this model. Stated differently, slowing of the flow during the interaction with the screen increases the interaction time, but also reduces the intensity of the interaction (reduces f_D), so there are competing effects at play in determining the integrated effect of the interaction.

Although there is reasonable agreement between the model and experimental results overall, the experimental results deviate from the model in interesting ways. Specifically, the model underpredicts ΔE for all conditions except the $\phi = 0.44$ results, in which case it overpredicts ΔE. One possible explanation for this trend is an interplay between the two terms in (4.11). For the cases with $\phi > 0.44$, the flow permeates the screen more rapidly, so a quadratic dependence of the drag force on the flow velocity might be expected, which is probably underestimated by the $\Delta IW_r/\phi$ term in (4.11), causing the model to underestimate ΔE for these cases. Conversely, the $\phi = 0.44$ results exhibit rapid deceleration due to the large blockage from the screen. The linear acceleration term represented by $-\Delta I/(2I_u)$ in the model is likely to underestimate this effect, causing the model to overestimate ΔE for $\phi = 0.44$. Higher-order effects are clearly important to capture all of the behaviour observed experimentally.

A more accurate description of the flow evolution could be obtained by modelling f_D directly. Given the definition of f_D, an appropriate model for this term would be $f_D = \Delta p$, where Δp is the pressure difference that develops across the screen during the interaction. Using this observation, it is tempting to approximate Δp using correlations for the pressure drop across thin screens in pressure-driven flows (such as Naaktgeboren 2007; Naaktgeboren, Krueger & Lage 2012). In pressure-driven flows, however, the flow speed does not adjust as the interaction progresses and energy dissipates, as it would in a momentum-driven flow. This is significant because correlations for pressure-driven flows place all of the ϕ dependence in velocity coefficients. To account properly for the ϕ dependence of momentum-driven flows, either the flow velocity also should have a ϕ dependence in correlations relating Δp to ϕ, or the slowing of the flow must be explicitly accounted for by applying a correlation for Δp obtained for pressure-driven flows as a function of time where the flow velocity used in the correlation is allowed to vary in time. The latter would require an iterative procedure, since Δp and the local flow velocity would be coupled, similar to (4.8). In any case, a local model for f_D would go a long way towards improving the current model by accounting for local variations in the flow interaction with the screen, especially radial variations in flow velocity.

5. Concluding remarks

The interaction of a vortex ring with a permeable screen orthogonal to the symmetry axis of the vortex ring shows remarkable similarity to the interaction of a vortex ring with a solid surface, even for screens with solid material occupying less than 50 % of their frontal area ($\phi > 0.5$). The usual features of increasing vortex ring diameter as it approaches the boundary, generation of secondary vorticity, and vortex rebound and reversal are all present for the case of a porous screen with sufficiently low ϕ. A key difference that appears in the case of the permeable screen is that, after the initial approach, the diameter of the incident ring begins to contract as fluid convects

through the screen and a downstream transmitted vortex is formed. The evolution of the secondary and tertiary vorticity is altered as a result, being drawn more towards the symmetry axis as well. All of these features are strongly dependent on ϕ, with trajectories approaching those for a solid boundary for small ϕ and very little effect on the flow trajectories for larger ϕ, as one would expect.

Similar to the flow kinematics, ϕ also had a dominant effect on the evolution of the flow dynamics, as expressed through the difference between the upstream and downstream hydrodynamic impulse and kinetic energy. The high-order influence of ϕ on kinetic energy is particularly noteworthy. Even for $\phi = 0.44$, nearly all of the kinetic energy was dissipated by the interaction of the vortex ring with the screen. Very large ϕ is required before the majority of the kinetic energy remains following the interaction. A somewhat smaller fraction of kinetic energy was dissipated when Re_j was doubled to 6000, but ϕ was still the primary factor determining kinetic energy dissipation. These observations suggest that large vortical structures would not easily survive in a distributed porous medium (e.g. several parallel screens) unless the energy of the incident vortex was very high or the porous medium was very porous. Conversely, it is apparent that even disperse obstructions can be effective at mitigating or controlling large-scale vortices appearing in non-uniform, unsteady flows.

For all cases considered in the present investigation, the screen wire diameter was small compared to the nozzle diameter of the vortex ring generator, and in the DPIV measurements, the screen wire diameter was held fixed for all ϕ considered. As the wire diameter increases, individual wires (not just the collection of wires represented by the screen) begin to become significant obstacles to the flow. The results of Hrynuk *et al.* (2012) indicate that the wire diameter can significantly affect the flow evolution, so in general both the bulk obstructive effect of the screen, represented by ϕ, and the form effect of the obstruction geometry need to be considered in determining the effect of the screen on the vortex ring.

Acknowledgement

This material is based upon work supported by the National Science Foundation under Grant No. 0347958.

REFERENCES

ADHIKARI, D. & LIM, T. T. 2009 The impact of a vortex ring on a porous screen. *Fluid Dyn. Res.* **41**, 051404.

BOLDES, U. & FERRERI, J. C. 1973 Behavior of vortex rings in the vicinity of a wall. *Phys. Fluids* **16**, 2005–2006.

CERRA, A. W. & SMITH, C. R. 1983 Experimental observations of vortex ring interaction with the fluid adjacent to a surface. *Tech. Rep.* FM-4. Lehigh University, Bethlehem, PA.

DOLIGALSKI, T. L., SMITH, C. R. & WALKER, J. D. A. 1994 Vortex interactions with walls. *Annu. Rev. Fluid Mech.* **26**, 573–616.

DYSON, F. W. 1893 The potential of an anchor ring. *Phil. Trans. R. Soc. Lond.* A **184**, 43–95.

HELMHOLTZ, H. 1867 On integrals of the hydrodynamical equations, which express vortex-motion. *Phil. Mag.* **33**, 485–512.

HRYNUK, J. T., VAN LUIPEN, J. & BOHL, D. 2012 Flow visualization of a vortex ring interaction with porous surfaces. *Phys. Fluids* **24**, 037103.

KRUEGER, P. S. 2006 Measurement of propulsive power and evaluation of propulsive performance from the wake of a self-propelled vehicle. *Bioinspir. Biomim.* **1**, S49–S56.

KRUEGER, P. S. & GHARIB, M. 2003 The significance of vortex ring formation to the impulse and thrust of a starting jet. *Phys. Fluids* **15**, 1271–1281.

LIM, T. T. & NICKELS, T. B. 1995 Vortex rings. In *Fluid Vortices* (ed. S. I. Green), pp. 95–153. Kluwer.

MAGARVEY, R. H. & MACLATCHY, C. S. 1963 The disintegration of vortex rings. *Can. J. Phys.* **42**, 684–689.

MAXWORTHY, T. 1972 The structure and stability of vortex rings. *J. Fluid Mech.* **51**, 15–32.

NAAKTGEBOREN, C. 2007 Interaction of pressure and momentum driven flows with thin porous media: experiments and modelling. PhD thesis, Southern Methodist University, Dallas, TX.

NAAKTGEBOREN, C., KRUEGER, P. S. & LAGE, J. L. 2006 Experimental investigation of vortex ring interaction with a permeable flat surface. In *Proceedings of the 3rd International Conference on Applications of Porous Media* (ed. A. Mojtabi & A. Mohamad), *ICAPM*, Paper No. 00015 (8 pp.).

NAAKTGEBOREN, C., KRUEGER, P. S. & LAGE, J. L. 2012 Inlet and outlet pressure-drop effects on the determination of permeabiliity and form coefficient of a porous medium. *Trans. ASME I: J. Fluids Engng* **134**, paper no. 051209.

NAAKTGEBOREN, C., OLCAY, A. B., KRUEGER, P. S. & LAGE, J. L. 2005 Vortex ring interaction with a permeable flat surface. *Bull. Am. Phys. Soc.* **50**, 165.

OLCAY, A. B. & KRUEGER, P. S. 2008 Measurement of ambient fluid entrainment during laminar vortex ring formation. *Exp. Fluids* **44**, 235–247.

ORLANDI, P. & VERZICCO, R. 1993 Vortex rings impinging on walls: axisymmetric and three-dimensional simulations. *J. Fluid Mech.* **256**, 615–646.

OSHIMA, Y. & ASAKA, S. 1977 Interaction of multi-vortex rings. *J. Phys. Soc. Japan* **42**, 1391–1395.

SAFFMAN, P. G. 1992 *Vortex Dynamics*. Cambridge University Press.

SHARIFF, K. & LEONARD, A. 1992 Vortex rings. *Annu. Rev. Fluid Mech.* **24**, 235–279.

STAYMATES, M. & SETTLES, G. 2005 Vortex ring impingement and particle suspension. *Bull. Am. Phys. Soc.* **50**, 165–166.

VERZICCO, R. & ORLANDI, P. 1996 Wall/vortex-ring interactions. *Appl. Mech. Rev.* **49**, 447–461.

WALKER, D. A. 1987 A fluorescence technique for measurement of concentration in mixing fluids. *J. Phys.* E: *Sci. Instrum.* **20**, 217–224.

WALKER, J. D. A., SMITH, C. R., CERRA, A. W. & DOLIGALSKI, T. L. 1987 The impact of a vortex ring on a wall. *J. Fluid Mech.* **181**, 99–140.

WESTERWEEL, J., DABIRI, D. & GHARIB, M. 1997 The effect of a discrete window offset on the accuracy of cross-correlation analysis of digital PIV recordings. *Exp. Fluids* **23**, 20–28.

WILLERT, C. & GHARIB, M. 1991 Digital particle image velocimetry. *Exp. Fluids* **10**, 181–193.

YAMADA, H., KOHSAKA, T. & YAMABE, H. 1982 Flowfield produced by a vortex ring near a plane wall. *J. Phys. Soc. Japan* **51**, 1663–1670.

YAMADA, H., MOCHIZUKI, O. & YAMABE, H. 1985 Pressure variation on a flat wall induced by an approaching vortex ring. *J. Phys. Soc. Japan* **54**, 4151–4160.